Materials and Structures (2026) 59:133
https://doi.org/10.1617/s11527-026-03025-4

ORIGINAL ARTICLE

Thermally induced moisture transport in concrete with different types of blended Portland cement studied by ^{1}H-NMR relaxometry

Tim Pittrich · Simon Peters · Günther Meschke · Frank Weise · Ludwig Stelzner

Received: 14 April 2025 / Revised: 21 November 2025 / Accepted: 19 February 2026 / Published online: 3 March 2026
© The Author(s) 2026

Abstract Clinker-reduced cements are gaining in popularity as part of efforts to lower the construction industry's CO_2 footprint. Past studies showed that utilization of these cements negatively influences the fire-induced spalling behavior of concrete, which is highly influenced by thermohydraulic damage mechanisms. Therefore, thermally induced moisture transport in normal strength concretes made with different types of blended cements (CEM I, CEM II/A-LL, CEM III/A and CEM II/B-Q) was investigated by means of ^{1}H-NMR relaxometry in combination with supportive side investigations concerning permeability and porosity. In addition, a numerical model was used to analyze in-situ moisture development during high temperature exposure. The results show that the cement type influences both initial moisture content and pore size-specific moisture distribution. This was primarily reflected in an increased water content in CEM III/A and CEM II/B-Q concretes as well as a comparable high gel pore water fraction in CEM II/B-Q concrete before heating. After heating, a similar degree of pore coarsening from gel to capillary pore was observed in all samples. Although the measurements were only conducted after, not during, high temperature exposure, the depth of the drying front and the extent of the moisture clog could be determined. With the additional numerical analysis, it can be assumed that during high temperature load, the drying front is less advanced and the moisture clog even more pronounced. In conclusion, it can be stated that the increased spalling susceptibility in blended cement concrete is caused by the lower initial permeability and increased moisture content.

Keywords Fire concrete spalling · Thermally induced moisture transport · Blended cements · ^{1}H-NMR

T. Pittrich (✉) · F. Weise · L. Stelzner
Bundesanstalt für Materialforschung und -prüfung, Berlin, Germany
e-mail: tim.pittrich@bam.de

F. Weise
e-mail: frank.weise@bam.de

L. Stelzner
e-mail: ludwig.stelzner@bam.de

S. Peters · G. Meschke
Institute for Structural Mechanics, Ruhr-Universität Bochum, Bochum, Germany
e-mail: simon.peters@rub.de

G. Meschke
e-mail: guenther.meschke@rub.de

1 Introduction

To reduce the construction industry's CO_2 emissions, more cements with a reduced clinker factor are finding application in infrastructure and residential construction. Therefore, the risk of low-carbon concretes being exposed to fire rises. Concrete under fire can experience heavy damage caused by explosive

spalling. Results of different research groups showed that the cement type influences spalling behavior; however, no clear relation between cement type and spalling susceptibility has been discovered [1]. Furthermore, there is even less knowledge available on the driving mechanism behind this phenomenon. Fire-induced spalling of concrete is usually caused by thermomechanical and thermohydraulic mechanisms. The thermomechanical spalling mechanism is based on restrained thermal expansion caused by the temperature gradient inside the concrete. The restrained thermal dilation causes high compressive stresses close to the fire-exposed surface, ultimately leading to tensile stress perpendicular to the heated surface, which is responsible for spalling [2, 3]. In addition, the thermal mismatch between expanding aggregates and shrinking cement paste (< 150 °C) [4] leads to the formation of microcracks, which further promote the risk of spalling [5, 6]. The thermohydraulic spalling mechanism was first mentioned by Shorter and Harmathy [7], who described water vapor migration and subsequent accumulation inside the concrete member, known as the moisture clog theory. The moisture clog, a saturated water layer caused by the condensation of water vapor in the concrete's cooler interior, inhibits any further moisture transport. Thus, pore pressure exceeding the tensile strength of concrete rises inside the concrete, causing high stresses which finally lead to explosive concrete spalling. However, the relation between pore pressure and spalling was never clarified and many other possible explanations of thermohydraulic spalling mechanisms have been summarized by McNamee [5]. A common strategy to avoid fire induced concrete spalling is the addition of polypropylene fibers (PP fibers) to the mixture. The PP fibers melt at around 170 °C, creating a network of empty fiber beds and mechanically-induced microcracks which allow water vapor to escape, reducing pore pressure [8].

To understand the impact of moisture on fire-induced spalling of concrete, different experimental studies in recent years have investigated heat-induced moisture transport, confirming the existence of the moisture clog. Neutron radiography studies in high performance cement mortar heated up to 600 °C showed a pronounced drying front as well as an increase in water content in regions where the temperature was close to 100 °C [9]. Further neutron tomography imaging of in-situ heated mortar specimens with superabsorbent polymers (SAP) and SAP in combination with PP fibers was conducted by Toropovs et al. [10]. The researchers investigated mortar slabs (25 × 100 × 100 mm) heated to 550 °C on a copper heating plate and simultaneously measured temperature, pore pressure and moisture content. The sample without PP fibers spalled at a depth correlating to the drying front, while the sample with PP fibers stayed unharmed. A noticeably smoother drying front was recorded for the PP fiber sample, indicating less steep temperature variations and therefore reduced thermal stress and pore pressure, minimizing the risk of spalling. Also, Dauti et al. [11] analyzed in-situ heat-induced moisture transport in high performance concrete (HPC) by means of neutron tomography. Two different mixtures with maximum aggregate sizes of 4 and 8 mm respectively were cast in cylindrical samples (d = 3 cm) and heated up to 300 °C. The drying front started to develop after 10 min at around 170 °C for both samples; however a faster-moving drying front for the sample with bigger aggregates was recorded. This faster drying was attributed to a more well-established crack network induced by the bigger aggregates. Beyond the drying front, water accumulation was visible in both samples at slightly different depths. X-ray tomography studies by Powierza et al. [12] led to similar results. The observations on HPC cylinders (h = 10; d = 4 cm) covered by a Marcor ceramic and aluminum silicate wool casting heated up to 300 °C showed once more the development of a drying front with subsequent appearance of the moisture clog. Van der Heijden et al. [13] used nuclear magnetic resonance (NMR) relaxometry to study the moisture distribution in concrete cylinders equilibrated at different relative humidities (97%, 86%, 75% and 50% RH) heated above 300 °C. The authors concluded that a comparable development of the drying front and condensation happened in all samples. However, only specimens cured at 97% RH and 86% RH reached a fully saturated state described as complete clogging. Furthermore, it was stated that neither the drying front nor condensation influence heat transport in the samples. The work by Stelzner et al. [14] considered heat-induced moisture transport measured by X-ray tomography as well as ^{1}H-NMR relaxometry in HPC cylinders with and without PP fibers equal to [12]. In both methods the development of the drying front and the moisture clog were detected when exposed to temperatures of 300 °C.

The addition of PP fibers led to a faster-moving drying front towards larger depths within the specimen, demonstrating their effectiveness by increasing the material's permeability. While X-ray tomography delivered a three-dimensional in-situ resolution of the moisture transport, NMR results only provided information on water distribution before and after heating. However, with the latter it was possible to quantify the absolute detectable water content as well as recording the reconfiguration processes of water from small to large pores. An overall evolution from fine to coarse pores between 200 and 800 °C was also observed in NMR studies by Guo et al. [15]. Chen et al. [16] investigated the in-situ permeability development of mortar and concrete made with CEM II/B-M (LL-S) and CEM V/A during heating to 60 °C, 105 °C and 200 °C. They concluded that moisture clogging depends on several factors including heating rate, sample scale, degree of saturation, and cement type. The researchers found that height-to-diameter ratios of approx. 2, heating rates between 2.5 and 4.9 K/min, and saturation levels starting at 45% were most critical for clogging. Moreover, it was observed that not only free water but also water released during dehydration of the cementitious matrix contributes to gas retention. Consequently, cement type plays a significant role in the clogging mechanism. Due to the higher thermal stability of CEM V cement paste, dehydration occurred more slowly, leading to a more uniform water release as temperature rises causing weaker gas retention. However, the higher initial saturation found in this type of mortar (exceeding 80%) ultimately also led to severe clogging.

In our previous work, noticeable differences in the spalling behavior of normal strength concrete with different types of blended cements were observed [17]. The spalling susceptibility of the concretes increased in the following order for the used cements CEM I (low), CEM II/A-LL (medium), CEM III/A (medium) and CEM II/B-Q (high) as displayed in Fig. 1. However, no information on the influence of the cement type on thermally induced moisture transport is available as most studies focus on concretes with Portland cement in HSC. Understanding moisture transfer in these concretes is particularly important as it is known that the binder type significantly influences both micro- and pore structure [18, 19] as well as the dehydration behavior of the cementitious matrix [20, 21]. Furthermore, as mentioned above, the utilization of clinker-reduced cements is increasing in practice. Against this background, the aim of this article is to fundamentally investigate the role of thermohydraulic spalling mechanisms in concretes with different types of blended cement. This work also covers the characterization of initial pore size distribution and evolution of the pore structure after heating. Based on the methodology of [14], ^{1}H-NMR relaxometry measurements were carried out on normal strength concretes made with four different types of cement before and after high temperature exposure. A numerical model was applied to simulate the course of the moisture transport during heating and

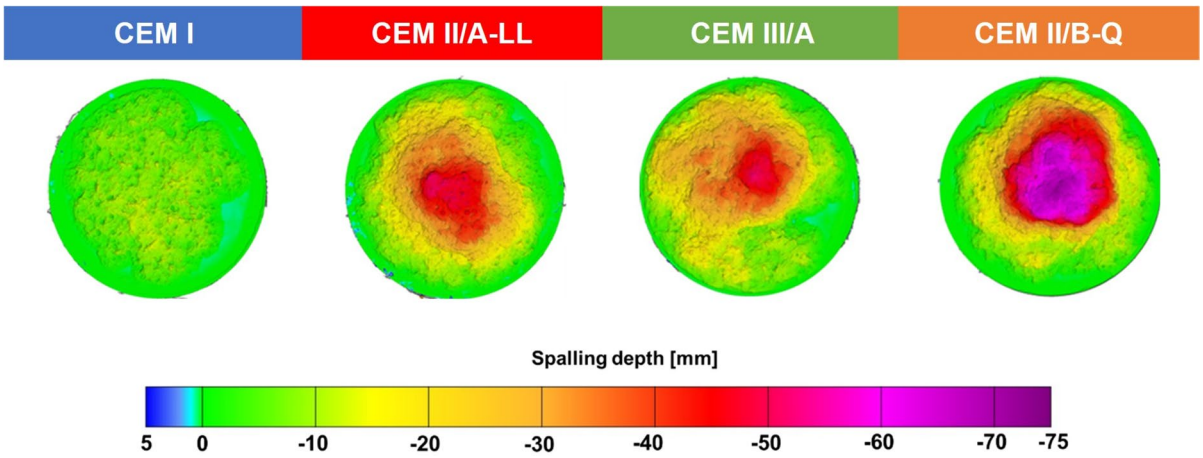


Fig. 1 Spalling depth of blended cement concretes after hydro-carbon fire exposure

Table 1 Main oxide composition of the cements (wt%)

Oxide	CEM I	CEM II/A-LL	CEM III/A	CEM II/B-Q
SiO_2	19.84	18.39	26.44	33.99
Al_2O_3	5.11	4.81	7.29	8.38
Fe_2O_3	2.99	2.66	1.91	3.00
CaO	61.87	60.68	52.47	45.58

Table 2 Blaine values of the cements (cm^2/g)

Cement	CEM I	CEM II/A-LL	CEM III/A	CEM II/B-Q
Blaine value	2900	4650	4890	6050

cooling which was not possible experimentally. In addition, porosity and gas permeability measurements were carried out to provide further information on the pore structure and transport properties.

2 Materials

Four cements, CEM I 42.5 N, CEM II/A-LL 42.5 N, CEM III/A 42.5 N, and CEM II/B-Q 42.5 N in accordance with DIN-EN 197 [22] and quarzitic aggregates were used for the casting of the concrete specimens. All cements contain clinker from the same production batch. A calcined clay with medium reactivity made of a kaolinitic-illitic clay was used for the production of CEM II/B-Q. To ensure a reasonable relation between aggregate size and sample diameter, the original mixture given in [17] with a maximum aggregate size of 16 mm was sieved down to 8 mm. Furthermore, polycarboxylatether-based (PCE) superplasticizer was needed to ensure comparable workability of the concrete with calcined clay cement (CEM II/B-Q) to the rest of the group. All concrete samples were demolded 1 d after casting. Subsequently the samples were stored under water for 6 more days and finally kept in a climate chamber at (20 ± 2) °C and (65 ± 5) % RH according to DIN EN 12390-2 [23] until an age of at least 90 d was reached, as recommended in [24].

The main oxide composition of the cements is given in Table 1, the Blaine values are provided in Table 2. The exact concrete composition and the corresponding fresh and hardened concrete properties of the original 16 mm mixture can be found in Tables 3 and 4. All the different concrete compositions are abbreviated in this paper as PC—Portland cement concrete, LC—limestone cement concrete, SC—slag cement concrete and CC—calcined clay cement concrete.

Table 3 Concrete composition (kg/m^3)

	PC	LC	SC	CC
Cement	420	420	420	420
Water (*w/c*)	197 (0.47)	197 (0.47)	197 (0.47)	197 (0.47)
Superplasticizer	0	0	0	2.5
Quarzitic aggregate				
0/2 mm	646	640	640	634
2/ 4 mm	153	152	152	150
4/ 8 mm	221	219	219	217
(8/16 mm)	(679)	(674)	(674)	(666)

Table 4 Fresh and hardened concrete properties for the concrete composition with 16 mm aggregates

Concrete	Fresh concrete properties	Hardened concrete properties			
	Slump flow (mm)	$f_{c,m}$ (MPa)		Bulk density (kg/m^3)	
		28 d	90 d	28 d	90 d
PC	445	46	50	2300	2300
LC	395	51	55	2330	2313
SC	418	57	59	2290	2310
CC	390	57	56	2317	2307

Three cylinders (drilled cores) with the dimensions h = 5 cm and d = 5 cm were used for gas permeability measurements. The same sample type was also utilized for porosity measurements determined by saturation with the help of the NMR tomograph. Lastly, mercury intrusion porosimetry (MIP) measurements were carried out on small concrete fragments.

To determine the thermally induced moisture transport, two samples of each concrete were prepared and measured by ^{1}H-NMR relaxometry. The fresh concrete was directly filled into slightly conic cylindrical glass–ceramic (Macor) casts and subsequently

densified on a vibrating table. This set-up was chosen to generate a 1D moisture transport, mimicking the conditions of a unilaterally-heated large scale concrete member.

3 Methodology

An overview of the methodology applied is given in Fig. 2. The first part of the main investigation includes analysis of the pore size-specific moisture distribution before and after unilateral heating in blended cement concretes by means of ^{1}H-NMR relaxometry. The second part describes the application of numerical simulations to understand the temporal course of local moisture distribution during heating and cooling. Moreover, supportive side investigations were conducted. Gas permeability measurements at room temperature and after defined high-temperature exposure provide additional information on the transport properties, supporting the interpretation of the moisture analysis by ^{1}H-NMR relaxometry. MIP in combination with ^{1}H-NMR relaxometry of pressure saturated samples was used to eliminate the effect of Fe_2O_3 on the NMR signal by estimating the corresponding surface relaxivity, which allows the conversion of measured transverse relaxation times into pore sizes (explained in detail in Sect. 3.5).

3.1 Gas permeability

The development of gas permeability was analyzed on three specimens of each concrete composition in the initial state and after temperature loading of 105 °C, 150 °C, 170 °C, and 300 °C. A moderate heating rate (approx. 1 K/min) was selected in order to minimize the risk of microcracks due to residual stresses caused by temperature gradients. The gas permeability coefficient was obtained at three different pressure states (3, 4, and 5 bar) using Ar based on the recommendations of RILEM TC 116-PCD [25]. Thereafter, intrinsic permeability, which is defined as apparent permeability extrapolated to infinite pressure, was determined in accordance with Klinkenberg [26].

3.2 Porosity

The concrete's porosity and pore size distribution were investigated by MIP in the initial state for

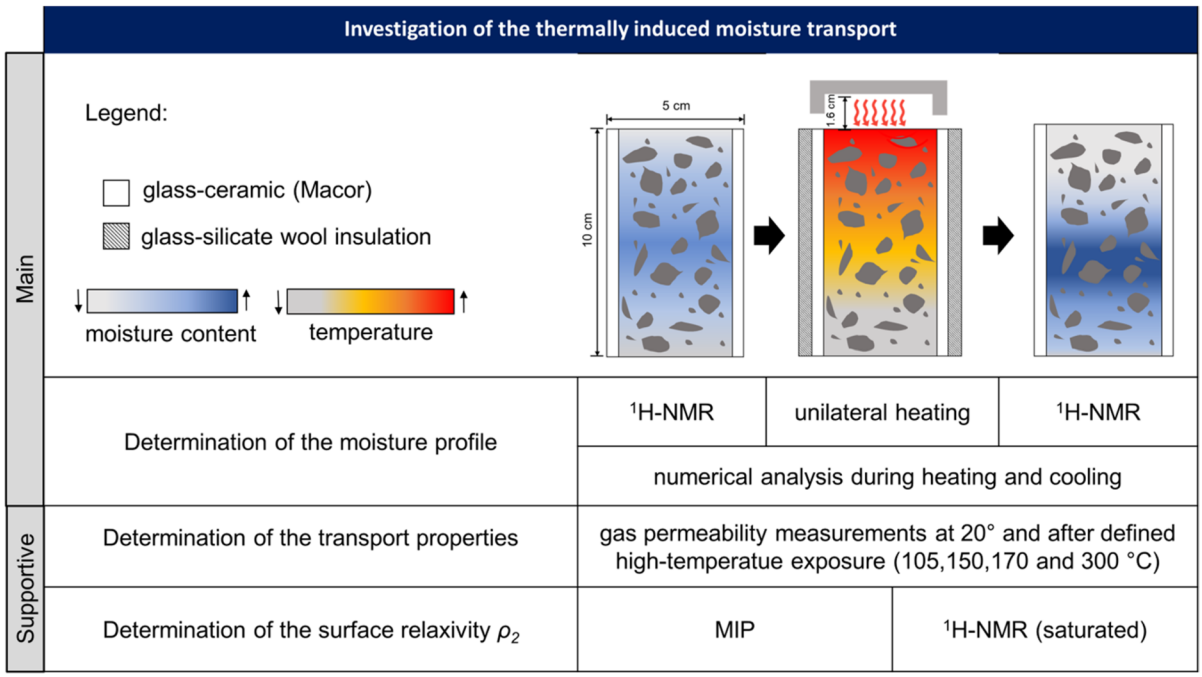


Fig. 2 Investigation program

two samples of each concrete. The porosimeter was operated in a pressure range of 0.0007–420 MPa with a chosen wetting angle of 140° according to ISO 15901-1 [27]. Throughout this paper the pore types are defined as gel pores ≤ 10 nm and capillary pores > 10 nm. Before measurement, the samples were vacuum-pulled and simultaneously dried at 40 °C for 24 h. It should be noted that thermal treatment may alter the pore structure, resulting in an increase of pore size and a higher proportion of capillary pores.

3.3 Unilateral heating

To analyze the thermally-induced moisture transport in the concretes, unilateral heating was applied. Since explosive concrete spalling usually occurs at temperatures around 300 °C, a surface temperature of 300 °C was targeted. This was achieved by using an equal experimental set-up as reported by Stelzner et al. [14], positioning an electrical heating device 1.6 cm above the specimen which was insulated by a glass-silicate wool covering. There was no contact between the sample and the device at any time, which led to heat transfer mainly conveyed by radiation. The heating rate was 10 K/min. Once the target value was reached after roughly 30 min, the temperature was held constant for 40 min. Next, the sample was allowed to cool freely within the room for 120 min. Right after, the sample was placed in the NMR-tomograph for the moisture distribution measurements. The temperature distribution in accompanying test specimens was also recorded.

3.4 Pressure saturation

The pressure saturation was carried out in accordance with [28]. First, the samples were placed under water and subjected to a vacuum with an absolute pressure ranging from 100 to 250 Pa for 3 h. Subsequently, the samples stayed under water at atmospheric pressure for an additional 2 h. Finally, the pressure was increased to 15 MPa, and the samples remained in the chamber for 24 h.

3.5 Experimental analysis of pore size-specific moisture distribution

Moisture content before and after heating was measured by ^{1}H-NMR relaxometry, a technique which allows the quantification of total water content and pore size-specific moisture distribution. An NMR core-analyzing tomograph (8.97 MHz) with a vertical resolution of 2 mm from pure devices GmbH was used; a detailed description of the tomograph and its capabilities can be found in [29]. A radio-frequency coil with a diameter of 52 mm was installed in the instrument. To study the transverse relaxation time (T_2) decay a Carr-Purcell-Meiboom-Gill (CPMG) pulse sequence was applied, where the corresponding echo time was 70 µs and the number of echoes was 1429 with a total of 200 scans per slice. Following the measurement, a multi-component T_2-time fitting was performed. This process is commonly referred to as an inverse Laplace transformation, although it more accurately involves solving a Fredholm integral equation of the first kind, where the measured signal is related to the T_2-time distribution through an exponential kernel [30]. The numerical inversion was performed using the software NucleusInv,[1] which employs lower–upper (LU) decomposition to ensure computational stability. A regularization parameter of $\lambda = 0.1$ (samples before and after heating) and 0.07 (pressure saturated samples) was applied to balance the trade-off between fitting accuracy and the smoothness of the resulting distribution. An exemplary illustration of the data inversion is provided in Fig. 3, including the measured data, the applied fit, and the resulting inversion.

The presence of magnetic impurities such as Fe_2O_3 influences the magnetic signal enhancing the T_2 decay, which causes a shift of the function to smaller T_2 times with increasing Fe_2O_3 content [31]. Hence, the translation of the T_2 time into pore sizes would lead to an overrepresentation of smaller pores. This is of particular importance as different cements with different Fe_2O_3 contents (see Table 1) are compared in this study. One possible way to eliminate this effect is given by estimating the surface relaxivity ρ_2 which describes the strength of the fluid's magnetic interaction with the surrounding pore walls. Thus, Eq. (1)

[1] https://github.com/ThoHiller/nmr-nucleus.

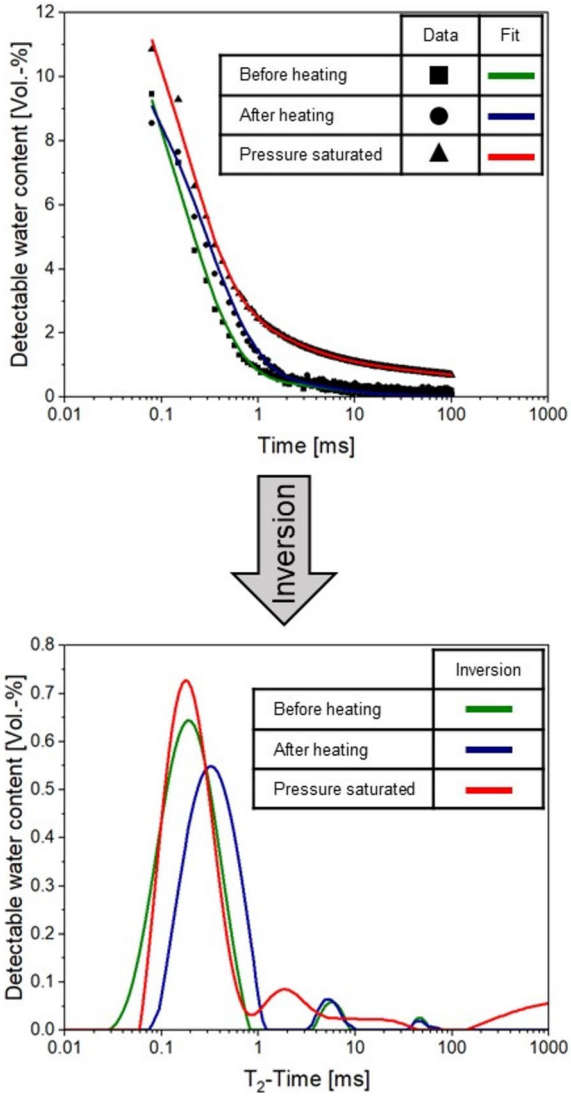


Fig. 3 Data inversion process (example CC)

allows the measured T_2 time to be directly assigned to the corresponding pore radius.

$$\frac{1}{T_2} = \rho_2 \frac{\alpha}{r} \tag{1}$$

where ρ_2 is the surface relaxivity, r is the pore radius, and α is the geometry shape factor. Depending on the pore geometry $\alpha = 1,2$ or 3 for planar, cylindrical or spherical shapes, respectively. To finally determine the surface relaxivity, porosity recorded by measuring vacuum-treated pressure-saturated samples by means of ^{1}H-NMR relaxometry were compared to porosities obtained by MIP. The area selected for curve fitting corresponds to the capillary pore space associated with the interhydrate pores of C-S-H. This region is identifiable as the most prominent capillary pore peak in the MIP curve and was chosen because it demonstrates the highest level of agreement between the measurement methods, as stated by Muller and Scrivener [32]. In this work, pore geometry is assumed to be cylindrical. This assumption arises due to the ink-bottle effect, which causes the MIP to predominantly detect pore throats, particularly in the smaller pore size range that accounts for the majority of the material's porosity. Therefore, the geometry shape factor of $\alpha = 2$ is used, which has also been applied in other studies [33, 34]. Subsequently, the surface relaxivity was chosen as the value leading to the best fit between NMR and MIP results. Once the surface relaxivity is acquired, Eq. 1 can be expressed as follows in Eq. (2), making the calculation of the pore radius in relation to the respective T_2 value possible.

$$r = \rho_2 \cdot a \cdot T_2 = \rho_2 \cdot 2 \cdot T_2 \tag{2}$$

3.6 Multiscale chemo-thermo-hygro-modeling

Due to the challenges associated with in-situ moisture content measurement during heating using NMR, assessments are typically conducted in the cold state. To reconstruct the evolution of the moisture front based on the experimentally obtained data, numerical modeling serves as a valuable tool and will be employed in the following analysis.

The numerical model is based on the hybrid mixture theory proposed by Lewis and Schrefler [35] describing cement-based materials as partially saturated porous media with a solid skeleton and an interconnected pore network containing capillary water, vapor, and dry air. It explicitly accounts for key high-temperature mechanisms, including temperature-dependent material properties, bound water release, phase transitions, and fluid transport. For heat and mass transfer in porous media, the model follows the Thermodynamically Constrained Averaging Theory framework [36], incorporating mass, energy, and momentum conservation at the continuum level. For

detailed formulations and governing equations, see Peters et al. [37, 38] .

The model incorporates four primary state variables: the temperature T, gas pressure p_g, capillary pressure p_c, and displacement field u, consistent with the formulation of Gawin and Pesavento [39] Additionally, five internal variables ξ_i describe the binder-specific dehydration kinetics, while a further internal variable, d, governs the evolution of mechanical damage.

The resulting governing system comprises ten coupled equations: mass balance for liquid water and dry air, an enthalpy balance (energy conservation), a momentum balance (mechanical equilibrium), and six evolution equations to capture the damage and dehydration processes. For completeness, the final form of the governing equations is presented below; a detailed derivation is provided in [40].

The enthalpy balance of the multiphase medium accounts for: (i) heat storage within the material, (ii) conductive heat transfer, (iii) latent heat effects associated with phase transitions, and (iv) heat release or consumption due to dehydration. It is expressed as in Eq. (3):

$$\left(\rho C_p\right)_{eff}\frac{\partial T}{\partial t} - \nabla\cdot\left(\lambda_{\text{eff}}\nabla T\right) = -\dot{m}_{\text{vap}}\Delta H_{\text{vap}} - \dot{m}_{\text{deh}}\Delta H_{\text{deh}} \tag{3}$$

where $(\rho C_p)_{\text{eff}}$ and λ_{eff} is the effective heat capacity of concrete and the effective thermal conductivity, respectively. ΔH_{vap}, ΔH_{deh} and m_{vap} are the enthalpy of evaporation dehydration, and the evaporated water mass, respectively [39].

The evolution of the solid density is governed by the temperature-dependent porosity according to [38] in Eq. (4):

$$\rho_s(T) = \rho_{s,0}\cdot\left(1-\phi_{p,\text{con}}\right) \tag{4}$$

In the proposed model, the porosity ϕ is not prescribed through an empirical function. Instead, it is directly linked to the dehydration kinetics of the individual hardened cement paste constituents via Eq. 3 The evolution of these constituents is described by five internal variables, each governed by its respective kinetic law, see [41]. Consequently, the cement paste porosity is expressed as in Eq. (5).

$$\phi = \phi_{\text{initial}} + \sum \phi_j \quad \text{with } \in \{\text{CH, AFt, TCA, AFm}_c\} \tag{5}$$

The mass balance of dry air accounts for diffusive and advective transport, as well as porosity variations induced by temperature, saturation changes, and density variations of water and air, leading to the following form in Eq. (6):

$$\frac{\partial\left(\phi(1-S)\rho_{\text{ga}}\right)}{\partial t} + \nabla\cdot\boldsymbol{J}_{\text{ga}} = 0 \tag{6}$$

where ρ_{ga} denotes the gas-phase density of air and J_{ga} the corresponding mass flux.

The mass balance of water (liquid and vapor) incorporates diffusive and advective transport of both phases, mass exchange induced by dehydration, and porosity variations arising from temperature changes, saturation evolution, and density variations of liquid water and water vapor. Accordingly, the governing Eq. (7) reads:

$$\frac{\partial\left(\phi(1-S)\rho_{gw} + S\rho_w\right)}{\partial t} + \nabla\cdot\left(\boldsymbol{J}_w + \boldsymbol{J}_b\right) = -\dot{m}_{\text{dehydr}} \tag{7}$$

where ρ_{gw} and ρ_w are the fluid densities and $(J_w + J_b)$ the fluid flux of water in gaseous and liquid state $\dot{m}_{\text{dehydr}}$ characterizes the source term from dehydration.

Fluid transport within the porous medium is governed by pressure-driven flow described by Darcy's law, while gas-phase diffusion and adsorbed water transport are modeled according to Fick's law [38]. These flux formulations enter the mass conservation equations introduced above. The resulting mass fluxes of dry air, water vapor, and liquid water are therefore given by Eq. (8)–(10):

$$\boldsymbol{J}_{\text{ga}} = -\frac{K_{\text{int},g}k_{rg}}{\mu_g}\nabla p_g - \frac{M_a M_w}{M_g^2}D_{\text{eff}}\nabla\left(\frac{p_{\text{ga}}}{p_g}\right) \tag{8}$$

$$\boldsymbol{J}_w = -\frac{K_{\text{int}}k_{rw}}{\mu_w}\left(\nabla p_g - \nabla p_c\right) - \frac{M_a M_w}{M_g^2}D_{\text{eff}}\nabla\left(\frac{p_{gw}}{p_g}\right) \tag{9}$$

$$J_b = -\boldsymbol{D}_b\nabla S_b \tag{10}$$

The multiscale framework of Peters and Meschke [41] is employed to determine binder-specific dehydration behavior and related pore space evolution at elevated temperatures, building on the stoichiometric formulas of each hardened cement paste constituent and the associated dehydration kinetic, governed by

an Arrhenius equation. Subsequently, at each temperature step the actual volume fractions of the constituents are utilized in a micromechanical framework to homogenize the effective macroscopic thermal conductivity; see Peters et al. [37] for further details.

In following numerical analysis, the initial thermal conductivity is calibrated based on the experimentally determined temperature field at depths of 5 mm, 10 mm, 20 mm, 30 mm, 50 mm, and 70 mm. Furthermore, the intrinsic permeability evolution is prescribed by the experiments conducted, see Fig. 4. All input parameters are summarized in Table 6, further material formulations can be found in Peters et al. [37].

4 Results

4.1 Permeability

The average intrinsic gas permeability and the maximum and minimum values determined after conditioning at different high temperature regimes are displayed in Fig. 4. First, it is noted that the PC sample exhibited an initial permeability almost half a magnitude higher than that of the other concretes. After exposure to 105 °C, all samples exhibited a similar increase in permeability. However, a further temperature increase to 150 °C led to a more pronounced permeability rise in CC and SC samples compared to PC and LC specimens. This trend continued for the final temperature steps of 170 and 300 °C and thus the final permeability of CC, SC and PC was equal while the LC showed a slightly lower value. Overall, the results show that with increasing temperature the initial differences in permeability between PC, SC, and CC vanish and ultimately reach the same value after exposure to 300 °C, while LC follows a weaker permeability development, ending at a slightly lower final permeability.

4.2 Porosity

Figure 5 shows the total cumulative porosity obtained by MIP, indicating comparable values for all concretes with 13.26, 13.21, 13.79, and 12.87 Vol.% for PC, LC, SC, and CC, respectively. A closer look into the specific pore sizes shows an equal distribution for PC and LC; the CC sample follows a similar course but exhibits less capillary porosity greater than 10 nm and an increasing number of gel pores down to 3.6 nm. The SC sample shows the lowest number of capillary pores over 30 nm but the highest number of small capillary and gel pores below this size. No significant differences in the pore size distribution above 200 nm were recorded.

4.3 Experimental analysis of pore size-specific moisture distribution

Moisture distribution before and after heating to 300 °C is displayed in Fig. 6. The surface relaxivities obtained were 6 nm/ms for PC, LC, and CC and 5 nm/ms for SC respectively (see Appendix A). In the initial state PC and LC exhibit a steeper drying gradient during conditioning in contrast to SC and CC concrete which finally reach similar depths of 20–30 mm. The absolute water content varied, as PC and LC specimens showed slightly lower total moisture contents of approximately 12 and 11 Vol.% compared to SC and CC which had a total amount of above 13 Vol.% detectable water. Furthermore, differences in the pore size-specific moisture distribution are visible, shown in Table 5. Most of the available water is found in the gel pores in every concrete. However, while PC and LC show comparable fractions of gel and capillary pores, SC shows the highest fraction of capillary pores above 10 nm. CC on the other hand

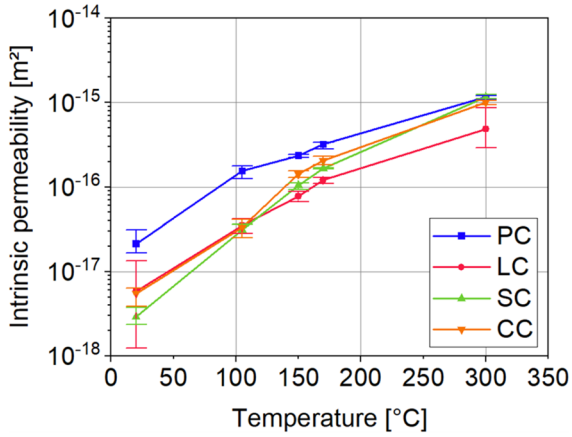


Fig. 4 Average intrinsic gas permeability of the different concretes before and after high-temperature exposure

shows the largest absolute and relative fraction of gel pores.

After heating the surface to 300 °C, a continuous drying front was established, and subsequently the appearance of the moisture clog was detected. Even though all the samples showed similar behavior, notable differences between the concrete types were obtained. Firstly, the drying front of the CC samples reached slightly deeper depths of around 50 mm in comparisons to roughly 40 mm for all other concretes. This corresponded to the steepest drying gradient found in the CC specimen. Furthermore, a more strongly developed moisture clog appeared in PC and LC compared to SC and especially CC. Lastly, moisture reconfiguration from gel pores to capillary pores happened in all specimens. While for the PC, LC, and SC samples, areas close to the beginning of the moisture clog experienced strong reconfiguration leading to more water found in capillary pores than gel pores, this is never the case for CC. Even though reconfiguration takes place, the gel pore fraction always contains the largest amount of water before as well as after high temperature exposure for this type of concrete.

A comparison of the one-dimensional moisture profiles after heating reveals three distinct zones, as shown in Fig. 7: dry, moist, and saturated (‘‘moisture clog’’). The dry zone extends from the top surface down to the point where the water content begins to rise sharply, marking the start of the moist zone. This moist zone ends at the onset of the moisture clog, which is defined here as the intersection between the post-heating water content and the initial water content. It is evident that all types of blended cement concrete exhibit a higher water content before the moisture clog, within a temperature range critical for explosive spalling. In other words, they contain more available thermal energy in the form of hot water in front of the impermeable zone. The lower permeabilities measured in blended cement concrete partly explain this phenomenon. However, the differences between the individual blended cement types cannot be attributed solely to variations in permeability, as those differences are comparatively small.

4.4 Numerical analysis of moisture distribution at elevated temperatures

To investigate the temporal saturation evolution of the different binder systems, the concrete samples have been discretized by 240 elements and analyzed by means of the multiphysics Finite-Element model described in Sect. 3.6. The input parameters are summarized in Appendix B Table 6, with the cement and concrete composition, permeability, and geometry matching experimental measurements. The

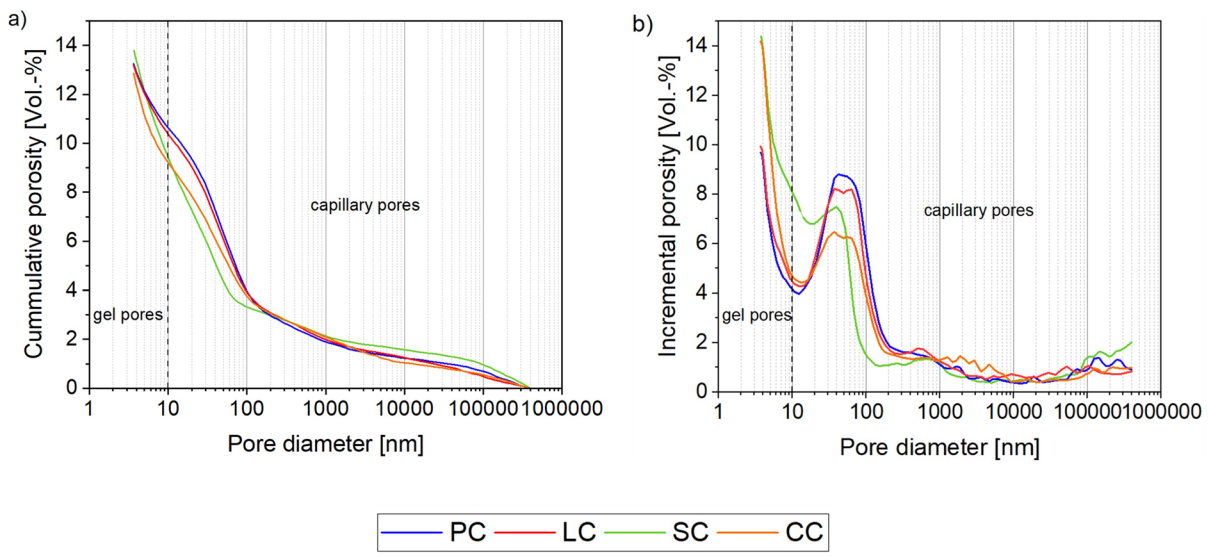


Fig. 5 Average porosity of the different concretes in the initial state **a** cumulative porosity; **b** incremental porosity determined by MIP

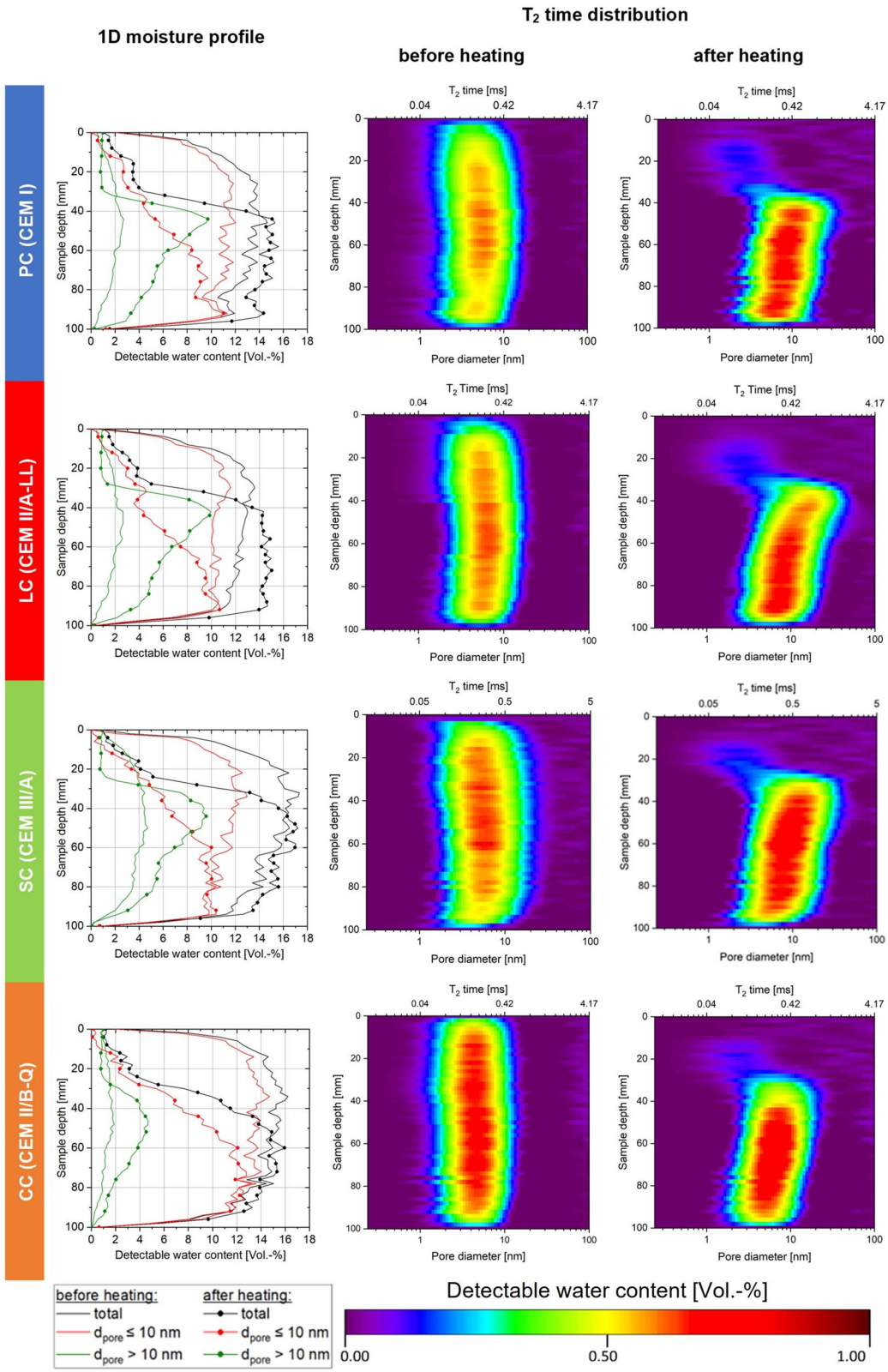
numerically computed temperature profiles at depths of 5 mm, 10 mm, 20 mm, 30 mm, 50 mm, and 70 mm are compared with the experimentally recorded temperatures in Fig. 8a, illustrating good agreement with the experimentally obtained data. The numerically determined moisture profiles represent the experimentally obtained data in Fig. 8 sufficiently, capturing both the individual drying depths and saturation curvatures in the drying zone. Rescaling the numerically determined saturation values into the detectable water content also shows good agreement between the calculated and experimentally determined depths and course of the curves after cooling (Fig. 8 b). This indicates that the qualitative moisture distribution during heating can be illustrated realistically.

Figure 9 contains computational results obtained from re-analyses of the ^{1}H-NMR experiment. It shows the saturation distribution along the depth of the specimen at different points of time during the uniaxial heating procedure protocol. The numerical analysis during the first 30 min of heating yields similar drying behavior for all concretes, see Fig. 9a. After reaching the target surface temperature of 300 °C at 30 min, a faster advancing drying front and lower moisture accumulation in deeper depths is observed for PC and LC as compared to SC and CC in Fig. 9b). On the other hand, the saturation increase behind the drying front remains similar for all concretes. At the start of cooling a more symmetric saturation profile is formed within moist zone for SC and CC as compared to PC and LC, see Fig. 9c. During the cooling phase, all saturation profiles exhibit a flattening effect, characterized by a reduced moisture gradient at the front, decreased saturation in the moist zone, and increased saturation in the previously dried regions, see Fig. 9d. Once again, an increased water content can be observed in front of the moisture clog in blended cement concrete, which is in alignment with the experimental results.

5 Discussion

The results show that the utilization of different blended cements affects concrete's microstructure and transport properties. Blended cement concrete with CEM II/A-LL, CEM III/A or CEM II/B-Q exhibits a lower initial permeability compared to CEM I samples. The increased fineness of the blended cements (Table 2) likely leads to a more densely packed microstructure, attributable to enhanced hydration kinetics and improved space-filling effects [42, 43]. Furthermore, binder-specific characteristics contribute to microstructural differences: in CEM II/A-LL concrete, the filler effect of limestone enhances packing density, while systems incorporating latent hydraulic or pozzolanic binders exhibit reduced portlandite and increased C-S-H contents, which may further densify the material. Moreover, Richardson and Groves [44] and Richardson [45] reported that the foil-like morphology of the outer product C-S-H in slag- or pozzolan-containing systems more efficiently fills space without leaving large interconnected capillary pores. Decreased pore connectivity in blended cement systems containing various types of SCMs has also been reported in other studies [46–49]. In addition, it was found that e.g. pozzolans have only little effect on mechanical properties, but significantly reduce pore connectivity compared to Portland cement [49]. The reduced connectivity limits the release of water vapor during fire exposure, which aligns with the low permeabilities observed in the blended cement concretes presented here. As a result, concrete of the same strength class may exhibit significantly varying spalling behaviors, as stated in this work. However, the permeability differences between CEM I, CEM III/A, and CEM II/B-Q become increasingly smaller above 105 °C and ultimately vanish at 300 °C.

The pore size-specific moisture distribution determined before and after heating by ^{1}H-NMR relaxometry showed that in the initial state, clear differences between the single binder types occur. In particular, the high initial moisture content in CEM III/A and CEM II/B-Q plus the large fraction of gel pore water in CEM II/B-Q, compared to OPC, should be highlighted. Moreover, pore coarsening takes place in all concretes during heating, leading to an increased amount of capillary water in the moisture clog regions after heating. The moisture profiles recorded after high temperature exposure show differences between the single blended concretes regarding the depth and extend of the moisture clog. However, the simulations suggest that these differences become more pronounced during cooling, leading to further movement of the drying front as well as to a decrease in the moisture clog. During heating, comparable depth and extent of the moisture clog are visible in all concretes. This shows that the ^{1}H-NMR measurements in


1D moisture profile
T2 time distribution
before heating
after heating
PC (CEM I)
LC (CEM II/A-LL)
SC (CEM III/A)
CC (CEM II/B-Q)
Sample depth [mm]
Detectable water content [Vol.-%]
T2 time [ms]
Pore diameter [nm]
before heating:
total
dpore ≤ 10 nm
dpore > 10 nm
after heating:
total
dpore ≤ 10 nm
dpore > 10 nm
Detectable water content [Vol.-%]
0.00
0.50
1.00

◂**Fig. 6** Moisture distribution and reconfiguration before and after heating determined by ^{1}H-NMR

the cold state after heating do not provide the moisture distribution which actually occurs during high temperature exposure. Therefore, the applied model turned out to be a valuable tool to close this gap of missing information.

The spalling behavior of the concretes can only be explained to a limited extent with the results presented. Firstly, the existence of the moisture clog was verified in every concrete, which is why a strong contribution of the thermohydraulic mechanism to the spalling can be assumed. However, one should not misinterpret the results by directly linking the depth of the moisture clog to the depth of spalling, since the damage was not caused by a single large spalling event but by many small events over a period of time. The lowest spalling tendency in CEM I concrete is most likely due to its low initial moisture content and comparatively high permeability before and during high-temperature loading leading to the fastest moving drying front. Despite comparable moisture content between CEM I and CEM II/A-LL concretes, the increased tendency to spall could be explained by the overall lowest permeability recorded over the entire temperature range. In CEM III/A concrete, the high initial moisture content appears to be responsible for the increasing spalling intensity. CEM II/B-Q concrete displays a similar high initial moisture content but additionally the highest proportion of gel pore water. Jiang et al. [50] reported that with decreasing pore radius, pore pressure rises inside concrete; this additional effect may lead to the most severe spalling observed in CEM II/B-Q concrete.

In summary, the increased spalling susceptibility of blended cement concrete can be attributed to the greater availability of thermal energy in the form of hot water within the moist zone preceding the moisture clog, which occurs in a temperature range critical for explosive spalling. This finding is supported by both experimental and numerical results. Lower permeabilities and higher initial moisture contents in blended cement systems are partly responsible for this appearance. However, the current data does not fully account for the differences observed among the individual blended concrete types.

The abovementioned findings suggest that the amount and nature of water, which is determined by the mineral phase composition, is decisive for thermohydraulic spalling. The dehydration and decomposition of the cementitious matrix determines the point of time and amount of water released under high temperature exposure. This also explains why CEM I and CEM II/A-LL concretes are quite similar in their pore structure and moisture distribution since they basically have the same mineral phase content. CEM III/A and CEM II/B-Q on the other hand include an additional component (slag or calcined clay) with an additional reaction mechanism (latent hydraulic or pozzolanic) strongly influencing the overall mineral composition in the non-hydrated and hydrated state. For example, it was observed that blended cement pastes with metakaolin or ground blast furnace slag showed larger amounts of C-S-H and calcium aluminate ferrite monosubstituted (AFm) phases but at the same time lower amounts of portlandite and calcium

Table 5 Average pore size specific moisture content (Vol.%)

Condition	Pore type	PC	LC	SC	CC
Before heating	Gel pores	10.09	9.39	10.12	12.04
	Capillary pores	1.62	1.61	3.28	1.15
	Total	**11.71**	**11.00**	**13.40**	**13.19**
After heating	Gel pores	5.75	5.57	6.49	7.52
	Capillary pores	4.08	4.45	4.61	2.23
	Total	**9.83**	**10.02**	**11.10**	**9.75**

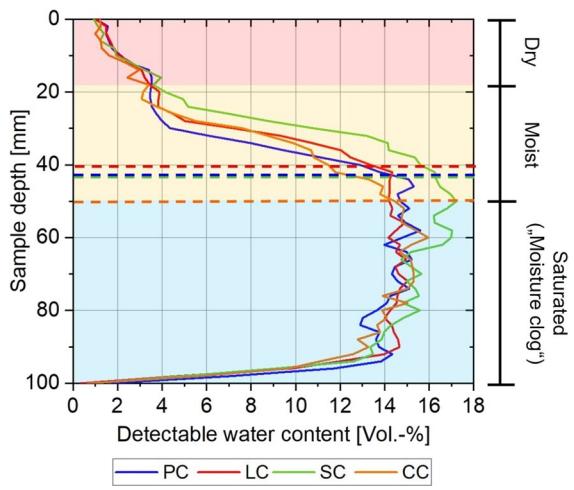


Fig. 7 Summarized illustration of the moisture distribution in the different types of concrete after heating showing an increased moisture content for blended cement concretes in the moist zone before the moisture clog. The dashed lines indicate the on-set of the moisture clog for the corresponding concrete

aluminate ferrite trisubstituted (AFt) phases compared to OPC cement pastes [51]. Furthermore, it has already been proven that low Ca/Si ratios promote Al uptake into C-(A)-S-H and subsequently higher Ca/Si and Al/Si ratios in the C-(A)-S-H phase generally lead to a denser foil like morphology [52]. Moreover, the water uptake increases in the C-(A)-S-H with introduction of Al to the system [52, 53], resulting in large amounts of non-evaporable gel water [52]. In addition to the C-S-H, the amount and type of AFt and AFm phases which are strongly dependent on the chemical composition of the cement [54] must not be neglected. It should be mentioned that these phases already start to decompose at approximately 70 °C and 170 °C, influencing the deterioration and dehydration of the microstructure at comparatively low temperatures. Furthermore, it cannot be ruled out that the different cement pastes have different thermal expansion behavior due to their compositional differences which could possibly lead to differing thermo-mechanical spalling behaviors.

Therefore, further investigations concerning mineral phase composition and their dehydration and decomposition behavior caused by high temperature exposure are planned for a better evaluation of thermally induced moisture transport of concretes with blended cements.

6 Conclusion

The investigations into thermally induced moisture transport in blended cement concrete led to the following conclusions:

- Initial permeability and porosity are influenced by the cement type. CEM I concrete shows the highest initial permeability in comparison to the other concretes made out of CEM II/A-LL, CEM III/A or CEM II/B-Q. The lower initial permeability in blended cement concrete in general appears due to increased fineness and improved hydration kinetics leading to a more efficient filling of the pore space. However, these differences strongly reduce with increasing temperature leading to an equal final permeability after an exposure to 300 °C in CEM III/A and CEM II/B-Q concrete.
- The initial moisture content is increased for CEM III/A and CEM II/B-Q. Additionally, these concretes show different pore size-specific mois-

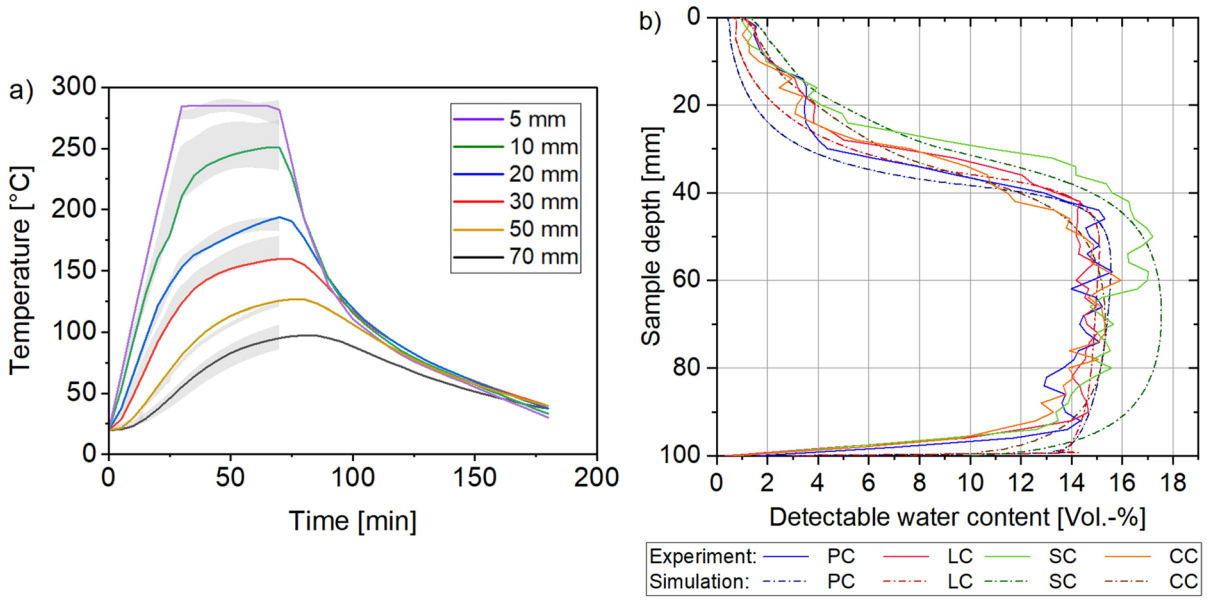


Fig. 8 **a** Numerically determined temperature profiles at depths of 5, 10, 20, 30, 50, and 70 mm for the heating and cooling procedure of 180 min. For comparison, the range of experimentally determined temperatures is included in the grey envelopes in the corresponding depths; **b** Experimental moisture distribution compared to simulated moisture distribution after 70 min of heating and subsequent cooling

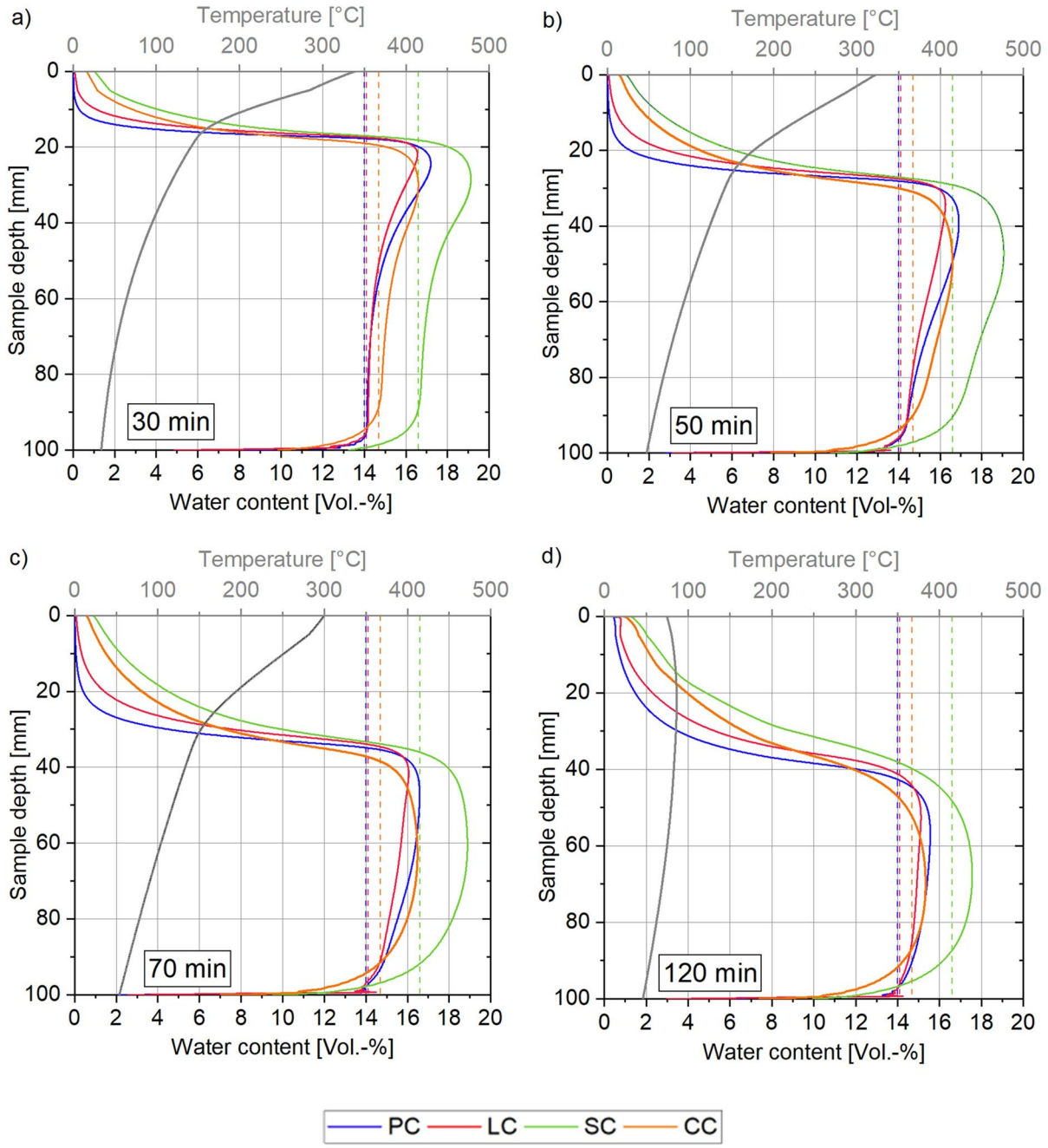


Fig. 9 Time-dependent moisture distribution during heating and cooling obtained by the numerical analysis **a** 30 min; **b** 50 min; **c** 70 min; **d** 120 min. Dashed lines indicate the initial water content of the corresponding concrete composition

ture distributions compared to CEM I and CEM II/A-LL concrete. CEM III/A exhibits the largest amount of capillary pore water while CEM II/B-Q exhibits the largest amount of gel pore water. This could affect the development of pore pressure.

- After temperature exposure, drying front and moisture clog formation in combination with pore coarsening were recorded in all specimens. However, there are clear differences in both the steepness of the drying gradient and the depth

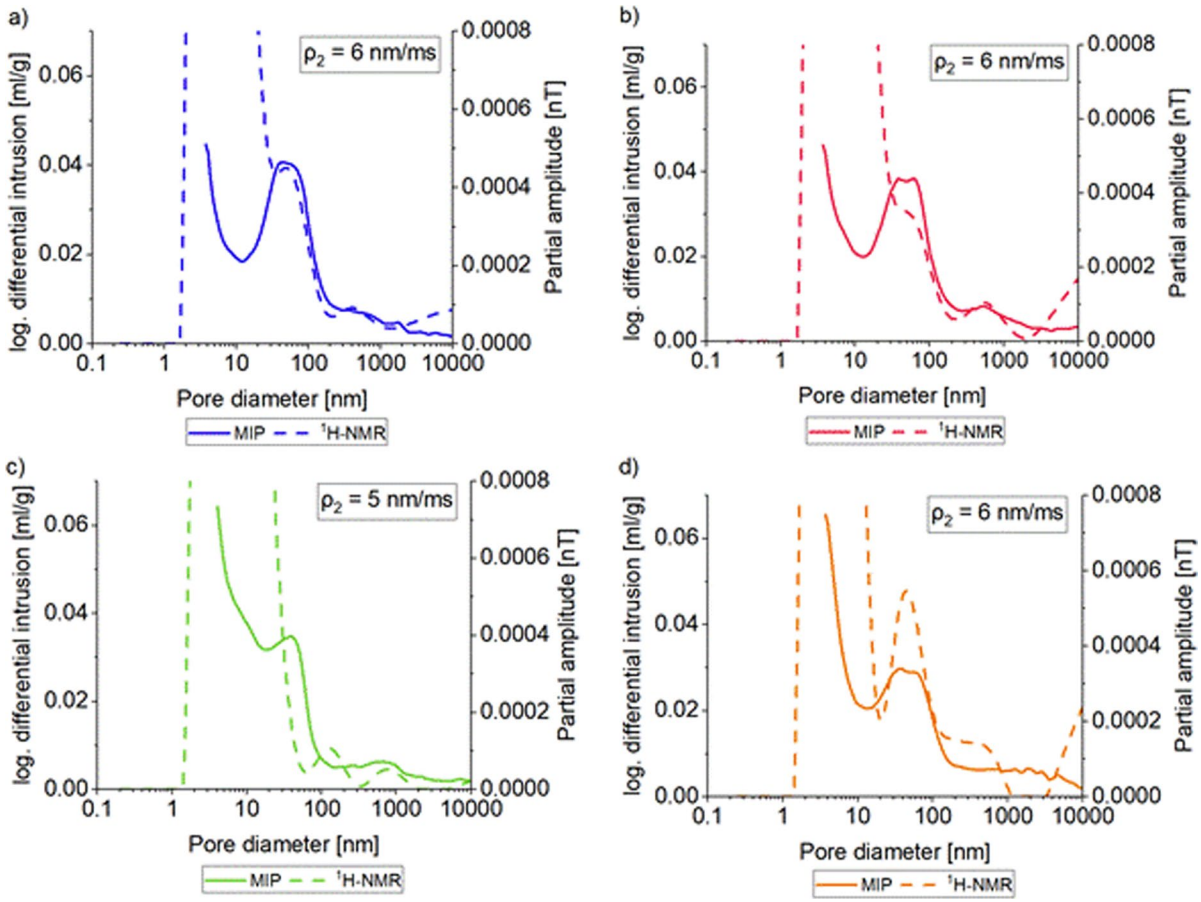


Fig. 10 Estimation of surface relaxivity ρ_2 by matching MIP and ^{1}H-NMR relaxometry results **a** PC; **b** LC; **c** SC; **d** CC

and extent of the moisture clog, which cannot be explained by permeability alone under the given circumstances.

- The simulation model presented shows a good agreement with the experimentally determined values. Additionally, it provides valuable insights into depth-resolved moisture development in the concrete specimen during heating and cooling. From these findings it can be concluded that the ^{1}H-NMR results after cooling are not entirely comparable with the moisture profile at the time of heating as they presented deeper depths of the drying fronts as well as lower water content of the moisture clog. Therefore, it serves as a valuable addition as it compensates for the weaknesses of the non-in situ high temperature measurement of ^{1}H-NMR.
- Blended cement concretes demonstrate higher spalling susceptibility due to the increased availability of hot water in the moist zone before the moisture clog. This relationship was confirmed through both experimental and numerical results. Responsible for this appearance are high initial moisture contents (CEM III/A and CEM II/B-Q concrete) as well as low permeabilities (CEM II/A-LL, CEM III/A and CEM II/B-Q concrete). The differences of spalling proneness between the single concrete types are not yet fully understood.

In the next step, investigations should be carried out at the level of mineral phase composition. Here the focus should be on the dehydration and decomposition behavior of the hardened cement paste after various high temperature loads to evaluate the phase changes, both qualitatively and quantitatively.

Acknowledgements We gratefully acknowledge the support of the German Research Foundation (DFG) and extend our gratitude for their financial support throughout the project

Table 6 Parameters utilized in the numerical analysis

Parameter	PC	LC	SC	CC
Permeability $K_{gas(20\ °C)}$	2.13e-17 (m^2)	5.86e-18 (m^2)	2.93e-18 (m^2)	5.47e-18 (m^2)
Permeability $K_{gas(105\ °C)}$	1.55e-16 (m^2)	3.49e-17 (m^2)	3.10e-17 (m^2)	3.31e-17 (m^2)
Permeability $K_{gas(150\ °C)}$	2.36e-16 (m^2)	7.69e-17 (m^2)	1.04e-16 (m^2)	1.43e-16 (m^2)
Permeability $K_{gas(170\ °C)}$	3.20e-16 (m^2)	1.20e-16 (m^2)	1.65e-16 (m^2)	2.05e-16 (m^2)
Permeability $K_{gas(300\ °C)}$	1.16e-15 (m^2)	4.88e-16 (m^2)	1.17e-15 (m^2)	9.99e-16 (m^2)
Permeability K_{int}	5e-20 (m^2)	5e-20 (m^2)	5e-20 (m^2)	5e-20 (m^2)
Saturation curve	$A_S = 86$ $B_S = 0.59$	$A_S = 86$ $B_S = 0.49$	$A_S = 86$ $B_S = 0.26$	$A_S = 86$ $B_S = 0.29$
$p_{c,initial}$	7.955e7 (Pa)	8.355e7 (Pa)	8.955e7 (Pa)	6.955e7 (Pa)
$p_{g,initial}$	101,325 (Pa)	101,325 (Pa)	101,325 (Pa)	101,325 (Pa)
$T_{initial}$	20 (°C)	20 (°C)	20 (°C)	20 (°C)
pbw	1:1.4:0.6	1:1.4:0.6	1:1.4:06	1:1.4:0.6
w/*c*	0.47	0.47	0.47	0.47
B_{sand}	0.56	0.56	0.56	0.56
$B_{aggregate}$	0.46	0.46	0.46	0.46
R (conductivity)	0.1	0.1	0.1	0.1

''Thermohydraulic spalling mechanisms in concretes with different binders with and without PP-fibers under fire exposure: An experimental and numerical analysis'' (Project Nr. 491928256). We also express our sincere appreciation to our colleagues, specifically acknowledging the collaborative efforts of BAM divisions 6.3: Structure Analysis, 7.1: Building Materials, and 7.4: Technology of Construction Materials. Their expertise and resources have significantly enriched the scope and depth of our study.

Funding Open Access funding enabled and organized by Projekt DEAL.

Data availability All data will be accessible upon request.

Declarations

Conflict of interest The authors declare that they have no known competing financial interests, personal relationships or any other affairs that could have appeared to influence the work reported in this paper.

Appendix A Estimation of surface relaxivity

Surface relaxivity was estimated by determining the best fit between MIP and ^{1}H-NMR results of pressure saturated samples. This method has already been used in the past in various studies dealing with the determination of fluid content in rocks, concrete or other building materials. Before comparing the samples, an equal sampling density for measurements is necessary. Therefore, the MIP pore size distribution was resampled to fit the NMR T_2-time distribution with a frequency of 30 points per decade. Subsequently, the surface relaxivity p_2 was chosen as the number providing the best match between the MIP and NMR curves displayed in Fig. 10.

Appendix B Simulation parameters and boundary conditions

For the simulation of the blended concretes the simulation parameters and initial conditions in Table 6 are conducted. For a detailed formulation of the constitutive laws, parametric relationships, and material parameter evolution, see [25, 26].

The boundary conditions are defined in accordance with the approach presented in Sect. 3.6 and remain consistent across all investigated cement types.

$$\left(\rho_{gw} v_g + \rho_w v_w + \rho_g v_{gw}\right)\boldsymbol{n} = \beta_c\left(\rho_{gw} - \rho_{gw,\infty}\right) \text{ on } \Gamma_c \tag{11}$$

$$\left(\rho_w v_l \Delta h_{\text{phase}} - \lambda_{eff} \nabla T\right) n = \alpha_c\left(T - T_\infty\right) + e\sigma_0 (T^4 - T_\infty^4) \tag{12}$$

Equation 11 is defined with capillary pressure parameters of β_c= 0.028 (ms^{-1}) on the heated side and β_c= 0.009 (ms^{-1}) on the rear side, with a gas–water equilibrium density of $\rho_{gw,\infty}$= 0.0031 (kg/

m^3) at both boundaries. Equation 12 governs the heat transfer on the rear side of the specimen, with convective heat transfer coefficient α_c= 8 ($Wm^{-2}K$) and radiation term $e\sigma_0 = 5.1e^{-8}$ ($Wm^{-2}K$). In addition to the Cauchy boundary conditions applied in Eqs. 11 and 12, Dirichlet boundary conditions are imposed for the pressure equation, setting the gas pressure to p_g = 101365 (Pa) on both sides. Furthermore, the temperature profile at depths of 5 mm, 10 mm, 20 mm, 30 mm, 50 mm, and 70 mm from the heated side is prescribed based on the data measured by the calibrated heater.

Open Access This article is licensed under a Creative Commons Attribution 4.0 International License, which permits use, sharing, adaptation, distribution and reproduction in any medium or format, as long as you give appropriate credit to the original author(s) and the source, provide a link to the Creative Commons licence, and indicate if changes were made. The images or other third party material in this article are included in the article's Creative Commons licence, unless indicated otherwise in a credit line to the material. If material is not included in the article's Creative Commons licence and your intended use is not permitted by statutory regulation or exceeds the permitted use, you will need to obtain permission directly from the copyright holder. To view a copy of this licence, visit http://creativecommons.org/licenses/by/4.0/.

References

1. Pittrich T, Weise F, Stelzner L (2025) The impact of blended cements on the spalling behavior of concrete at elevated temperatures: a review. Mater Struct. https://doi.org/10.1617/s11527-025-02713-x
2. Bažant Z P (1997) Analysis of Pore Pressure, thermal Stredd and Fracture in Rapidly Heated Concrete. International Workshop on fire Performance of High-Strength Concrete. Gaithersburg
3. Ulm FJ, Coussy O, Bazant ZP (1999) The "'Chunnel"' fire I: chemoplastic softening in rapidly heated concrete. J Eng Mech 125:272–282. https://doi.org/10.1061/(ASCE)0733-9399(1999)125:3(272)
4. Schneider U (1982) Behaviour of Concrete at High Temperatures Deutscher Ausschuss für Stahlbeton, pp 1–110
5. McNamee R (2019) Fire Spalling Theories—Realistic and More Exotic Ones. In: Proceedings of the 6th International Workshop on Concrete Spalling due to Fire Exposure. Sheffield
6. Peters S, Vu G, Meschke G (2025) A multiscale model for predicting the Young's modulus and the thermal-expansion coefficient of concrete at high temperatures. Constr Build Mater. https://doi.org/10.1016/j.conbuildmat.2025.141259
7. Shorter GW, Harmathy TZ (1961) Discussion on the Fire-resistance of prestressed concrete beams, pp 313–315
8. Pistol K, Weise F, Meng B et al (2011) The mode of action of polypropylene fibres in high performance concrete at high temperatures. In: 2nd International RILEM Workshop on Concrete Spalling due to Fire Exposure. Delft, pp 289–296
9. Weber B, Wyrzykowski M, Griffa M et al (2013) Neutron radiography of heated high-performance mortar. MATEC Web of Conferences vol 6
10. Toropovs N, Lo Monte F, Wyrzykowski M et al (2015) Real-time measurements of temperature, pressure and moisture profiles in high-performance concrete exposed to high temperatures during neutron radiography imaging. Cem Concr Res 68:166–173. https://doi.org/10.1016/j.cemconres.2014.11.003
11. Dauti D, Tengattini A, Dal Pont S et al (2018) Analysis of moisture migration in concrete at high temperature through in situ neutron tomography. Cem Concr Res 111:41–55. https://doi.org/10.1016/j.cemconres.2018.06.010
12. Powierza B, Stelzner L, Oesch TS et al (2019) Water migration in one-side heated concrete: 4D in-situ CT monitoring of the moisture-clog-effect. J Nondestruct Eval 38:66
13. Van der Heijden GHA, Pel L, Adan OCG (2012) Fire spalling of concrete, as studied by NMR. Cem Concr Res 42:265–271. https://doi.org/10.1016/j.cemconres.2011.09.014
14. Stelzner L, Powierza B, Oesch T et al (2019) Thermally-induced moisture transport in high-performance concrete studied by X-ray-CT and ^{1}H-NMR. Constr Build Mater 224:600–609. https://doi.org/10.1016/j.conbuildmat.2019.07.065
15. Guo J, Tian W, Cheng X et al (2024) Study on the evolution of concrete pore structure and moisture transfer mechanism after high temperature based on different sequence NMR technology. Constr Build Mater. https://doi.org/10.1016/j.conbuildmat.2024.135739
16. Chen X-T, Rougelot T, Davy CA et al (2009) Experimental evidence of a moisture clog effect in cement-based materials under temperature. Cem Concr Res 39:1139–1148. https://doi.org/10.1016/j.cemconres.2009.07.015
17. Pittrich T, Stelzner L, Weise F (2024) Fire-induced spalling of normal strength concrete with different types of blended Portland cement. In: The 13th International Conference on Structures in Fire. Coimbra, pp 451–461
18. Wu K, Shi H, Xu L et al (2016) Microstructural characterization of ITZ in blended cement concretes and its relation to transport properties. Cem Concr Res 79:243–256. https://doi.org/10.1016/j.cemconres.2015.09.018
19. Berodier E, Scrivener K (2015) Evolution of pore structure in blended systems. Cem Concr Res 73:25–35. https://doi.org/10.1016/j.cemconres.2015.02.025
20. Deschner F, Winnefeld F, Lothenbach B et al (2012) Hydration of Portland cement with high replacement by siliceous fly ash. Cem Concr Res 42:1389–1400. https://doi.org/10.1016/j.cemconres.2012.06.009

21. Mendes A, Sanjayan J, Collins F (2008) Phase transformations and mechanical strength of OPC/Slag pastes submitted to high temperatures. Mater Struct 41:345–350. https://doi.org/10.1617/s11527-007-9247-8
22. DIN EN 197-1 (2011) Cement-Part 1: Composition specifications and conformity for common cements, Beuth Verlag GmbH, Berlin
23. DIN EN 12390-2 (2019) Testing hardened concrete—Part 2: Making and curing specimens for strength tests, Beuth Verlag GmbH, Berlin
24. Pimienta P, McNamee R, Hager I et al (2023) Recommendation of RILEM TC 256-SPF on the method of testing concrete spalling due to fire: material screening test. Mater Struct. https://doi.org/10.1617/s11527-023-02202-z
25. RILEM TC 116-PCD (1999) RILEM TC 116-PCD: Permeability of Concrete as a Criterion of its Durability. Materials ans Structures 32:174–179
26. Klinkenberg LJ (1941) The Permeability of Porous Media to Liquids and Gases. Production Practice, pp 200–213
27. International Organization for Standardization (2016) Evaluation of pore size distribution and porosity of solid materials by mercury porosimetry and gas adsorption—Part 1: Mercury Porosimetry (ISO Standard No. 15901-1)
28. Bunke N (1991) Prüfung von Beton—Empfehlungen und Hinweise als Ergänzung zu DIN 1048. Deutscher Ausschuss für Stahlbeton. https://doi.org/10.2366/3708068
29. Kruschwitz S, Munsch S, Telong M et al (2023) The NMR core analyzing tomograph: a multi-functional tool for non-destructive testing of building materials. Magn Reson Lett 3:207–219. https://doi.org/10.1016/j.mrl.2023.03.004
30. Fordham EJ, Enkataramanan L, Mitchell J et al (2017) What are, and what are not, Inverse Laplace Transforms. J Basic Princ Diffus Theory, Exp Appl. https://doi.org/10.62721/diffusion-fundamentals.29.952
31. Schulte Holthausen R, Raupach M (2018) Determination of porosity and pore size distribution in concrete by single-sided ^{1}H NMR—From white cement pastes to grey cement mortars. IBAUSIL: Weimar, pp 595–603
32. Muller ACA, Scrivener KL (2017) A reassessment of mercury intrusion porosimetry by comparison with 1H NMR relaxometry. Cem Concr Res. https://doi.org/10.1016/j.cemconres.2017.05.024
33. Zhao P, Wang L, Xu C et al (2020) Nuclear magnetic resonance surface relaxivity and its advanced application in calculating pore size distributions. Mar Pet Geol 111:66–74. https://doi.org/10.1016/j.marpetgeo.2019.08.002
34. She AM, Yao W, Yuan WC (2012) Evolution of various states of water in blended cementitious materials. Appl Mech Mater 193:389–392. https://doi.org/10.4028/www.scientific.net/AMM.193-194.389
35. Lewis R, Schrefler BA (1998) The Finite Element Method in the Static and Dynamic Deformation and Consolidation in Porous Media. John Wiley and Sons, Hoboken
36. Hassanizadeh M, Gray WG (1979) General conservation equations for multi-phase systems: 1. Averaging procedure. Adv Water Resour 2:131–144
37. Peters S, Pittrich T, Stelzner L et al (2025) Model based evaluation of effects of the composition of CO2 -reduced blended concrete on the chemo-thermo-hygral behavior at elevated temperatures. Cement Concr Compos. https://doi.org/10.1016/j.cemconcomp.2025.106163
38. Gawin D, Majorana B, Schrefler B (1999) Numerical analysis of hygro-thermic behavior and damage of concrete at high temperature. Mech Cohesive-Frict Mater 4:37–74
39. Gawin D, Pesavento F (2012) An overview of modeling cement based materials at elevated temperatures with mechanics of multi-phase porous media. Fire Technol 48:753–793. https://doi.org/10.1007/s10694-011-0216-y
40. Gawin D, Pesavento F, Schrefler BA (2003) Modelling of hygro-thermal behaviour of concrete at high temperature with thermo-chemical and mechanical material degradation. Comput Methods Appl Mech Eng 192:1731–1771. https://doi.org/10.1016/S0045-7825(03)00200-7
41. Peters S, Meschke G (2024) Computational multiscale modelling of thermallyinduced dehydration of blended hardened cement paste. Cem Concr Res. https://doi.org/10.1016/j.cemconres.2024.107485
42. Sugrañez R, Álvarez JI, Cruz-Yusta M et al (2013) Controlling microstructure in cement based mortars by adjusting the particle size distribution of the raw materials. Constr Build Mater 41:139–145. https://doi.org/10.1016/j.conbuildmat.2012.11.090
43. Bentz DP, Garboczi EJ, Haecker CJ et al (1999) Effects of cement particle size distribution on performance properties of Portland cement-based materials. Cem Concr Res. https://doi.org/10.1016/S0008-8846(99)00163-5
44. Richardson IG, Groves GW (1992) Microstructure and microanalysis of hardened cement pastes involving ground granulated blast-furnace slag. J Mater Sci 27:6204–6212
45. Richardson IG (1999) The nature of C-S-H in hardened cements. Cem Concr Res 29:1131–1147
46. Ranger M, Tange Hasholt M (2023) Relationship between chloride migration, bulk electrical conductivity and formation factor of blended cement pastes. Nord Concr Res 69:33–53. https://doi.org/10.2478/ncr-2023-0009
47. Higuera-Flórez C, Cárdenas-Pulido J, Lizarazo-Marriaga J et al (2023) Implementation of the formation factor (F) to evaluate properties of cement-based materials from electrochemical techniques. 2023 Congreso Internacional de Innovación y Tendencias en Ingeniería (CONIITI). Bogotá, pp 1–6. https://doi.org/10.1109/CONIITI61170.2023.10324013
48. Yio MHN, Wong HS, Buen NR (2019) 3D pore structure and mass transport properties of blended cementitious materials. Cem Concr Res 117:23–37. https://doi.org/10.1016/j.cemconres.2018.12.007
49. López M, Castro JT (2010) Effect of natural pozzolans on porosity and pore connectivity of concrete with time. Rev Ing Constr 25:419–431
50. Jiang W, Zhang D, Zheng X et al (2023) Development of pore pressure in cementitious materials under low thermal effects: evidence from optimization of pore structure by incorporation of fly ash. Materials. https://doi.org/10.3390/ma16124214
51. Saillio M, Baroghel-Bouny V, Bertin M et al (2019) Phase assemblage of cement pastes with SCM at different ages.

Constr Build Mater 244:144–157. https://doi.org/10.1016/j.conbuildmat.2019.07.059
52. Kapeluszna E, Kotwica Ł, Rózycka A et al (2017) Incorporation of Al in C-A-S-H gels with various Ca/Si and Al/Si ratio: microstructural and structural characteristics with DTA/TG, XRD, FTIR and TEM analysis. Constr Build Mater 155:643–653. https://doi.org/10.1016/j.conbuildmat.2017.08.091
53. Myers RJ, L'Hôpital E, Provis JL et al (2015) Effect of temperature and aluminium on calcium (alumino)silicate hydrate chemistry under equilibrium conditions. Cem Concr Res 68:83–93
54. Matschei T, Lothenbach B, Glasser FP (2007) The AFm phase in Portland cement. Cem Concr Res 37:118–130. https://doi.org/10.1016/j.cemconres.2006.10.010

Publisher's Note Springer Nature remains neutral with regard to jurisdictional claims in published maps and institutional affiliations.